J Solid State Electrochem (2008) 12:47–55
DOI 10.1007/s10008-007-0332-2

ORIGINAL PAPER

Double template electrochemical deposition and characterization of NiCo and NiCu alloys nanoparticles and nanofilms

Adolphe Foyet · Anton Hauser · Wieland Schäfer

Received: 11 December 2006 / Revised: 15 March 2007 / Accepted: 2 April 2007 / Published online: 8 May 2007

Abstract The principle of double template deposition technique was developed to prepare NiCo and NiCu alloy nanomaterials. Ordered particles of about 800 nm high were obtained by reduction of ions from aqueous solution into the pores of anodic aluminum oxide (AAO) membrane with intact barrier layer. The size of the nanoparticles was significantly reduced by combination of AAO and the hexagonal phase of a lyotropic liquid crystal. The scanning tunneling microscopy (STM) micrograph of the material prepared in the presence of liquid crystal reveals the hexagonal array of cylindrical pores. The corrosion potential of the alloy nanofilm shifted to more negative values when the sizes of the particles decrease. The anodic linear sweep voltammetry shows, in each case, various current peaks characteristic of the dissolution of chemical elements in the film.

Keywords Alloy nanomaterials · Liquid crystal · Corrosion · Impedance

Introduction

Nanomaterials have attracted extensive interest in recent year because of their fundamental properties and wide range of applications. Cobalt- and nickel-based alloys are particularly attractive due to their magnetic properties. Electrodeposited magnetic films have applications in computer read/write heads and microelectromechanical systems [1]. Moreover, possible applications include magnetic recording media, sensors [2], and giant magneto resistance from CoCu, FeAg, and CoAg multilayers [3]. In biomedical applications, the use of nanoparticles that present super paramagnetic behavior at room temperature is desired [4].

The binary alloy CuNi shows a promising magnetic phase transition in the desired range of temperature for hyperthermia treatment of cancer [5]. Macroscale electrodeposition of CoNi- and CoFe-based magnetic films was investigated by Myung et al. [6]. Report exists also on CuCo thin film [7] or multilayers [8] prepared by electrochemical method and CoCu alloys by physical vapors deposition [3].

To increase the storage density of semiconductor memories, the sizes of each memory cell must be reduced. A smaller memory cell also leads to faster speeds and lower power consumption [9]. Numerous deposition techniques have been developed to prepare nanomaterials, among them, template synthetic method using highly ordered alumina membrane [10–12]. Pores of size ranging between 10 and 300 nm diameter can be prepared by electrochemical anodization of aluminum [13]. Nanostructured material with particle size smaller than 5 nm was also deposited from a lyotropic liquid crystalline phase of non-ionic surfactants [14–16].

In this work, we report on the electrochemical deposition and characterization of NiCo and NiCu alloy mesoporous films by single and double template methods. Each alloy nanofilm was first prepared by electrochemical reduction of ions dissolved in the appropriated aqueous solution within the pore of a thin anodic aluminum oxide (AAO). Secondly, the hexagonal phase of a lyotropic liquid crystal containing metallic ions was combined with the AAO for deposition. Two different types of surfactants molecules were used: a

A. Foyet · A. Hauser · W. Schäfer (✉)
Institut für Physikalische Chemie,
Martin-Luther-Universität Halle-Wittenberg,
Kurt-Mothes-Strasse 2,
06120 Halle (Saale), Germany
e-mail: wieland.schaefer@chemie.uni-halle.de

non-ionic surfactant with larger columns (larger diameter) and an ionic surfactant with smaller columns. The aim was to show the effect of the plating mixture (diameter of the columns of surfactant) on the size of the nanoparticles. The electrochemical properties of the mesoporous films are also investigated.

Experimental

The thin AAO used for the experiment was prepared by a modified two-step anodization described by Masuda and Fukada [17]. The aluminum foil was electropolished with 15 V_{DC} for 3 min in a mixture of 25 vol.% $HClO_4$ and 75 vol.% ethanol. Anodization was performed during 30 min in 0.3 M oxalic acid at 10 °C with 40 V_{DC}. The first anodic film formed by this method was removed at 60 °C in a mixture of 0.2 M CrO_3 and 0.4 M H_3PO_4. The foil was anodized again for 30 min. The perforated AAO remains on the aluminum foil; all depositions were made with the intact barrier layer.

The hexagonal phase of lyotropic liquid crystals was prepared according to the method described by Attard et al. [18, 19]. The first plating mixture consists of 60 wt% Polyoxyethylene(20)stearyl-ether (Acros organics Brij78, $C_{18}EO_{20}$) and 40 wt% of aqueous solution containing 0.11 M $CoSO_4$, 0.11 M $NiSO_4$, 0.2 M H_3BO_3, and 0.1 M ascorbic acid (mixture A) in the case of NiCo alloy film. The aqueous solution contains 0.025 M $CuSO_4$, 0.22 M $NiSO_4$, and 0.2 M H_3BO_3 (mixture B) in the case of NiCu alloy. For each alloy, the second liquid crystal template has 50 wt% of hexadecyltrimethyl–ammonium bromide (Acros organics ionic surfactant; CTAB) and 50 wt% of mixture A or B.

All electrochemical depositions were conducted using potentiostat/galvanostat model 273A (PAR EG&G Princeton Applied Research) with two electrodes consisting of Al_2O_3/Al (WE with a geometric area of 0.5 cm^2) and platinum foil (CE). A saturated calomel electrode (RE) was introduced during corrosion and impedance measurements.

The liquid crystal Brij78 was melted at 55 °C within the pores of AAO while CTAB was heated to 30 °C during deposition. At these temperatures, each liquid crystal remains in the hexagonal phase. The direct current motor controller micropositionner C-842.20 (Physik Instrumente with a transmission ratio of 118.6 count/μm) was used to maintain the distance between the WE and CE at about 2± 0.1 mm. This facilitates the electrical conduction (particularly in the case of Brij 78 non-ionic mixture) and the reproducibility of the experiment. A thermoelectric module (Peltier element 193585-ZA) was mounted under the WE to regulate the temperature. After deposition, the surfactant was removed by soaking the electrode in distilled water for at least 6 h; during this time, the water was replaced every 2 h. At the end, the electrode was cleaned with distilled water, dried in air, and submitted to AFM or STM analysis.

The electrochemical impedance spectroscopy (EIS) spectra were measured with a lock-in amplifier model 5210 (PAR EG&G) coupled with the potentiostat. The measurements were carried out in 0.4 M $LiClO_4$ over the frequency range from 100 kHz to 5 Hz (10 points per decade) using 5 mV amplitude of sinusoidal voltage.

The atomic force microscope (AFM) and scanning tunneling microscope (STM) instruments (TopoMetrix TMX 2010 Discoverer) were used to analyze the surface of the deposits. All AFM images are topographies (without filter) recorded in non-contact mode (cantilever resonance frequency 321 kHz) with a silicon tip. Gausian filter was applied to STM images to eliminate noise. All images were analyzed with WSxM© (http:// www.nanotec.es) 4.0 Develop 7.1 image browser scanning probe software.

Results and discussion

Template electrochemical deposition

The electric parameters have been varied to obtain homogeneous deposition of particles in the pore of alumina membrane with intact barrier layer. In general, high current density and short deposition time are necessary for electron to tunnel across the small barrier layer of the alumina membrane and to achieve homogeneous deposition of particles. This will be easy if the thickness of the porous anodic film is very small. Deposition of particle in alumina membrane with intact barrier layer is advantageous, as the samples are easy to handle and offer the possibility of large-scale deposition and industrial application.

Figure 1a shows the AFM micrograph of the porous alumina membrane on aluminum. A thin AAO film is expected when the anodization time (30 min×2) is very short. The under barrier layer of such membrane should be small, and it could allow electrons to tunnel across; this will favor the electrodeposition of material in the pore of AAO with intact barrier layer. The thickness of the porous alumina template is less than 60 nm as shown on the profile. But this value may not be exact, as the AFM tip cannot go deeper in the pore to measure the real thickness of the sample. The real thickness should be several times larger than the observed value.

Figure 1b and c shows the topography of NiCo and NiCu films deposited from mixture A and B, respectively. It appears that the pores of this membrane are filled in homogeneous manner by metal particles. The periodicity (center-to-center spacing between two neighboring NiCo or NiCu alloy particles) determined by line measurement and

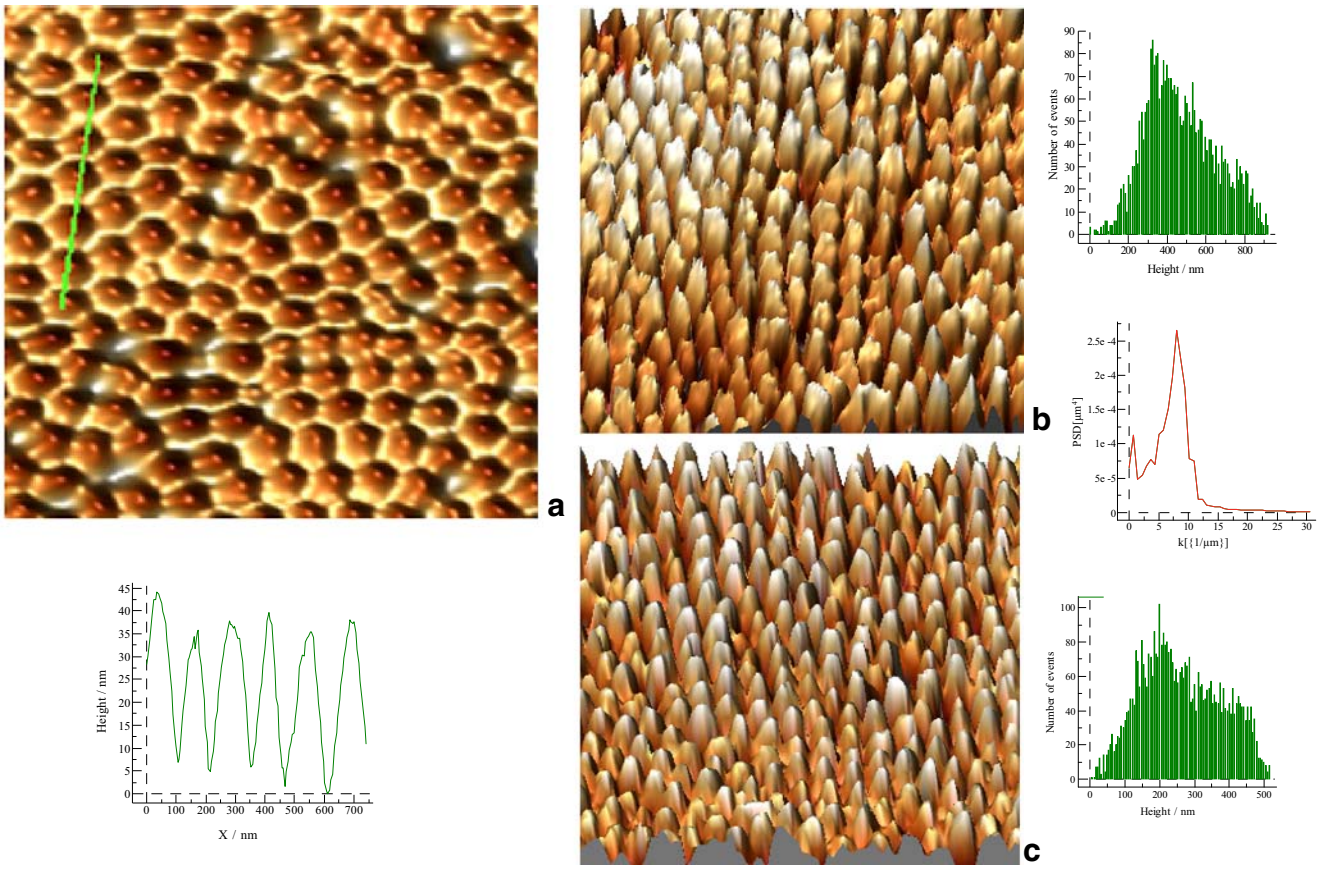

Fig. 1 Structures of AAO membrane (**a**), NiCo (**b**), and NiCu (**c**) alloy nanorods obtained from aqueous solution; the deposition charges were 0.9 Coulomb for **b** and 0.7 Coulomb for **c**. The current density was 2.5 mA/cm^2 in both **b** and **c** cases. Each picture is 1.6×1.6 μm. The power spectra density function (*PSD*) shows a peak at the wavelength that corresponds to the repeat distance

2D Fourier transformed (PSD spectrum) is about 120 nm. The average height of the samples is 500 and 300 nm for NiCo and NiCu film, respectively. The histogram of size distribution shows, in each case, the number of particles and their specific length. It is possible to grow particles of about 800 nm in length in the pores of AAO.

The surface-to-volume ratio is very high in nanoparticles; hence, surface effects play an important role in determining the physical properties of a film [4]. In addition, the plasmon resonance modes can be tailored by varying the structural features, sizes, and spacing of the metallic nanostructured film [20, 21]. To reduce the size of particles and increase the specific area of the film, a hexagonal phase of liquid crystals (Brij 78 or CTAB) was combined with the AAO as template for deposition. The repeat distances in Brij 78 and CTAB hexagonal mixture are about 8.2 nm [22] and 3.5 nm [23] respectively, while the diameter of the pore of AAO is about 55 nm. We expect that many columns of surfactant could penetrate in one pore of AAO; after deposition and removal of the liquid crystal, the film should have many pores.

Figure 2a and b shows the structures of NiCo and NiCu alloy nanofilm prepared in the presence of Brij 78 liquid crystal mixture. The samples have double substructures: one due to the pore of aluminum oxide membrane that direct the fibers from the bottom to the top of the pores; the second subdivision is caused by the columns of liquid crystal that divide the nanorods into many small particles. The profile along the line shows clearly the subdivisions of the particles. The STM images confirm the presence of small pores on the material.

The CTAB molecule is smaller than the Brij 78; therefore, the diameter of the columnar phase (about 3.5 nm) is also very small. The nanopores created in the metal film by this surfactant cannot be resolved with AFM instrument operating with a 10-nm Tip. The STM instrument operating in constant current mode with platinum–iridium tip was used to analyze the films deposited in the presence of this plating mixture.

Figure 3a and b shows the topographies of NiCo and NiCu films deposited with CTAB liquid crystal mixture. In both cases, the material is highly porous. Figure 3c depicts the 2D structure of the mesoporous film in the hexagonal pore of AAO (see hexagon) and the expected nanostrucuture of the material caused by the columns of CTAB. In general, many small particles exist in each pore of the AAO. The

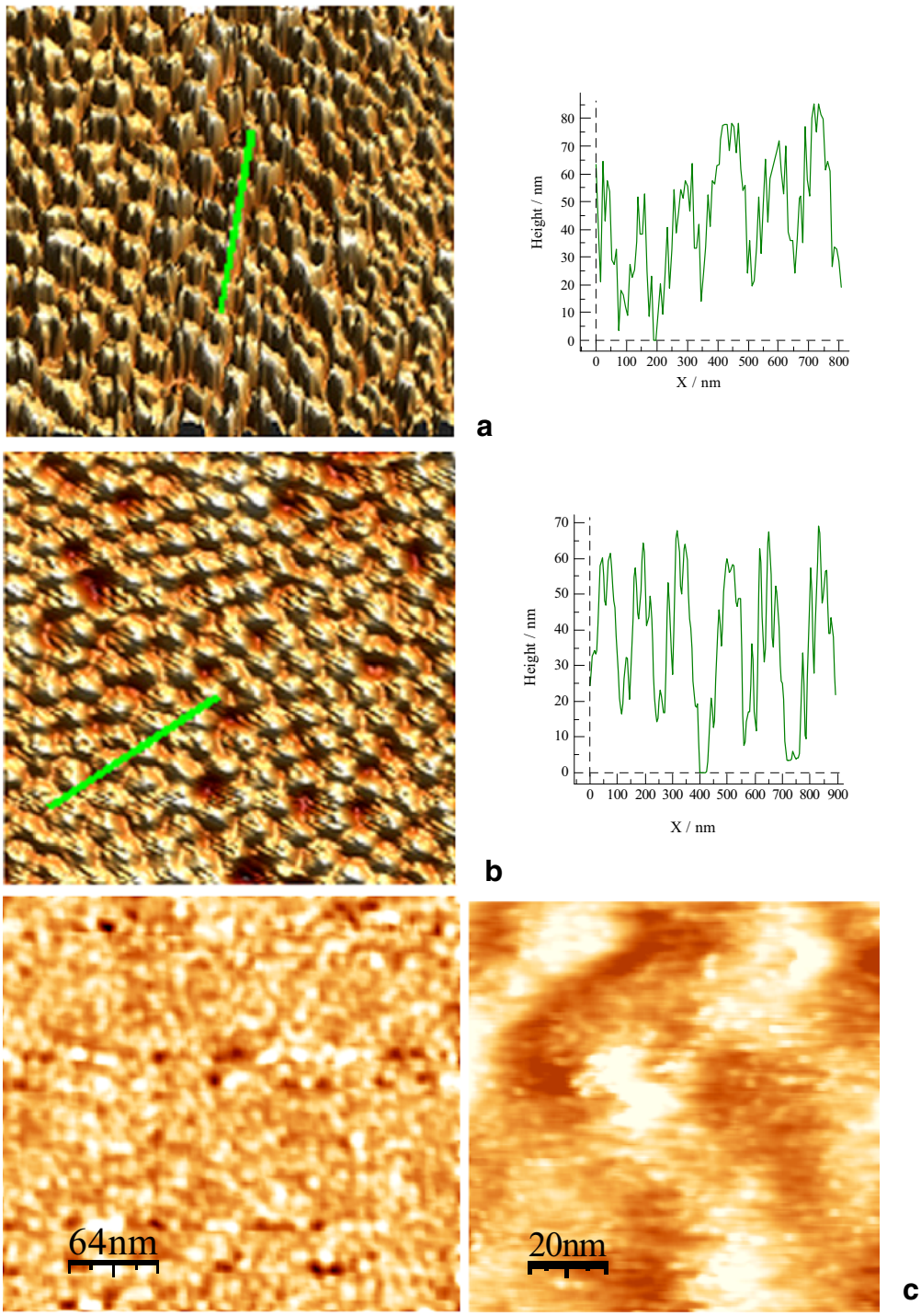

Fig. 2 AFM micrograph of NiCo (**a**) and NiCu (**b**) nanofilm prepared by combination of Brij 78 liquid crystal and AAO (double template deposition). Quantity of electricity, 0.5 C for **a** and 0.4 C for **b**. The profile along the *line* shows the subdivisions of the particles. **a** and **b** are $1.6 \times 1.6\ \mu m^2$. The STM micrographs of the samples are shown in **c**

high resolution of the mesoporous film is represented in Fig. 3d. This STM micrograph reveals the hexagonal array of cylindrical pores with nearly uniform size. 2D Fourier transformation was used to determine the periodicity in the structure; the power spectra density function (PSD; Fig. 3e) shows a peak at the spatial wavelength characteristic of the repeat distance. The inter-pores distance obtained by this method is 4.35 nm, a value close to the repeat distance (3.5 nm) of the hexagonal CTAB mixture. This confirms the templating effect of the surfactant.

The porosity of NiCo and NiCu magnetic nanofilms increases significantly when these materials are prepared in the presence of surfactant. Both Brij 78 and CTAB gave nanostructured films with two repeat distances. The first periodicity is that between the pores of AAO, while the small columns of surfactants cause the second subdivisions.

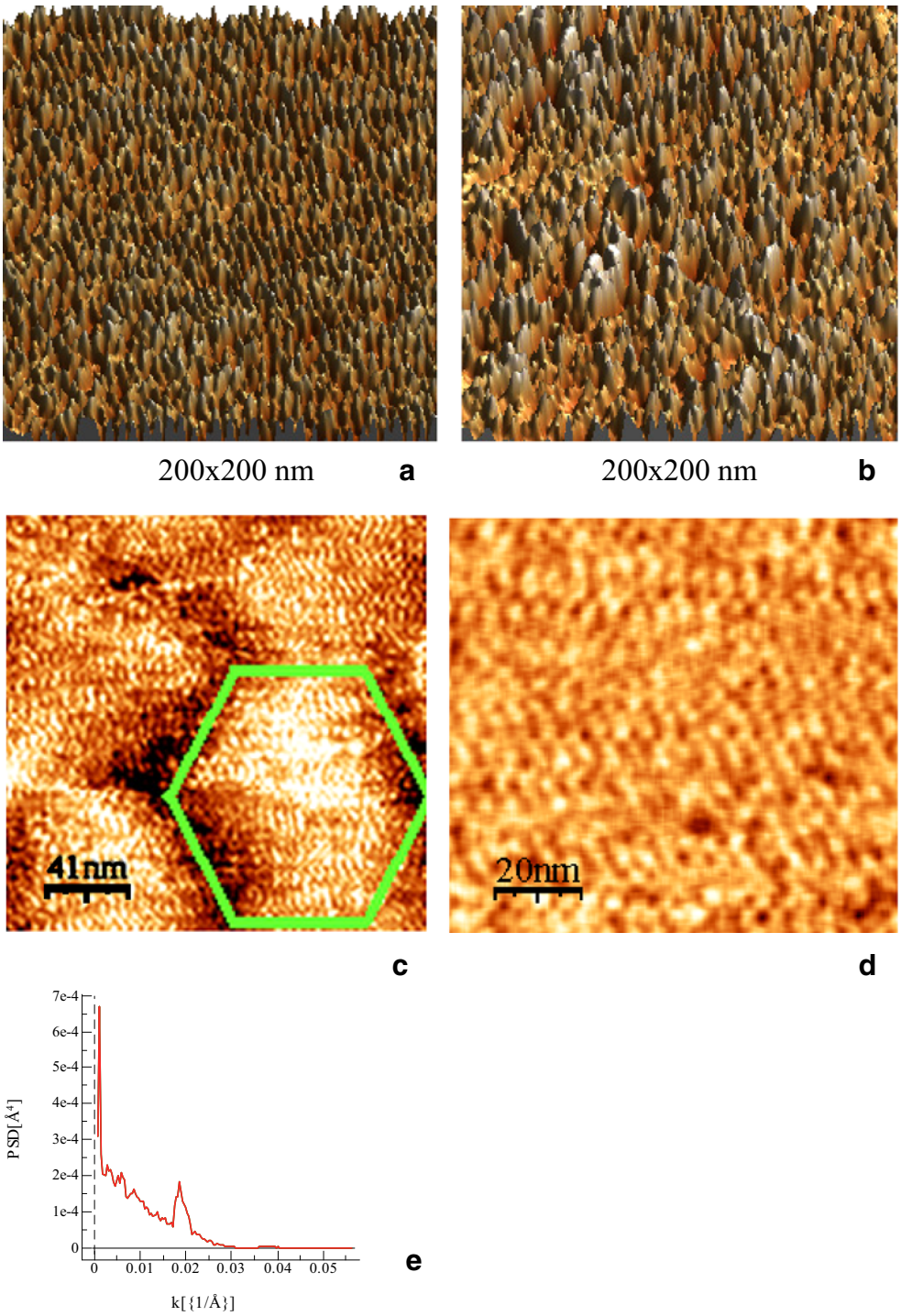

Fig. 3 Structure of NiCo (**a**), NiCu (**b**) deposited in the presence of CTAB liquid crystal. **c** The 2D of a similar structure showing the structure caused by the pores of AAO (*hexagon*) and the subdivisions due to CTAB columns. **d** The high resolution of image **c** and **e** the power spectra density with a peak at the wavelength characteristic of the repeat distance. Noises were removed in all pictures with four matrix points Gausian filter

Therefore, the double template process increases the specific area of the film and may also improve the physical and chemical properties of these nanomaterials.

Polarization behavior

The constituents of each alloy film were investigated by potentiodynamic striping in 0.4 M $LiClO_4$ aqueous solutions. Voltammetry techniques were proven to be the convenient electrochemical methods of characterrization of the phase structure of alloy [24]. In particular, anodic linear sweep voltammetry gives various current peaks; peaks are characteristic of dissolution of chemical elements or phase transition in the alloys.

The polarization curve of NiCo, NiCu alloy and Ni films under quasi-equilibrium conditions exhibits distinct active and passive regions. The departure of the active dissolution of the film is the point where the current begins to raise; in

this region, an oxide film grows on the electrode surface. Passivation is reached when the oxide covers completely the electrode surface, and the electrical conduction is both electronically and ionically.

The polarization curve of NiCu alloy nanoparticles exhibits two anodic peaks that can be attributed to the successive oxidation of nickel and copper. The high intensity of the peak at 0.2 V (Fig. 4a) shows that the copper content of the alloy is greater than the nickel concentration. The passivation of the film occurs at potential greater than 0.5 V vs SCE. In the metallurgical point of view, NiCu is well known as typical single-phase alloys for all alloy composition and temperature. Therefore, the existence of two peaks on the polarization curve of this alloy should not be assigned to phase transition.

The presence of two peaks in the case of NiCo may also account for successive oxidation of nickel and cobalt. The oxidation peaks of Fig. 4b are close to each other, as the difference in redox potential of Ni^{2+}/Ni (−0.23 V vs SHE) and Co^{2+}/Co (−0.28 V vs SHE) is very small. The peaks may also account for the existence of two phases in the alloy. It is well known that in the binary Ni–Co phase diagram, the system forms solid solutions with fcc structures in the range Co/(Ni + Co)=0–0.75 at room temperature and that the system transforms to an hcp structure in the range Co/(Ni + Co)=0.75–1 [25]. Nickel and cobalt have a very close atomic radius (0.15 and 0.16 Å, respectively), and cobalt exist in both fcc and hcp structure; cobalt atom can easily take the position of nickel in the crystal structure and vice-versa. It has been reported that various phase separations (e.g., Co-rich Co–Ni hcp and Ni-rich Ni–Co fcc) tend to occur even in the composition range where fcc structures are normally formed [25].

In the present work, the chemical composition and phase were not easy to determine because a material with very fine structure was prepared on aluminum, and the thickness of the film (<1 μm) was small. The total amount of metal present in the form of thin film is in the range of microgramme; these made the analysis of the composition and phase very difficult. Nevertheless, it is expected from the principle of galvanostatic co-deposition of ions (used in the present case) that Ni and Co should be present in the form of alloy on the aluminum surface. Therefore, the existence of two peaks in the polarization curve of this material may account for the selective dissolution of its elements or for the presence of two phases if we take in consideration the remarks of [25] mentioned above.

Figure 4c depicts the polarization curve of Ni film deposited in the same conditions like the NiCo and NiCu film. The curve shows an active dissolution in the potential region from −1 to −0.5 V vs SCE follow by a passive regions (−0.15 V≤E≤0.6 V) and a transpassive region at potentials greater than 0.7 V vs SCE.

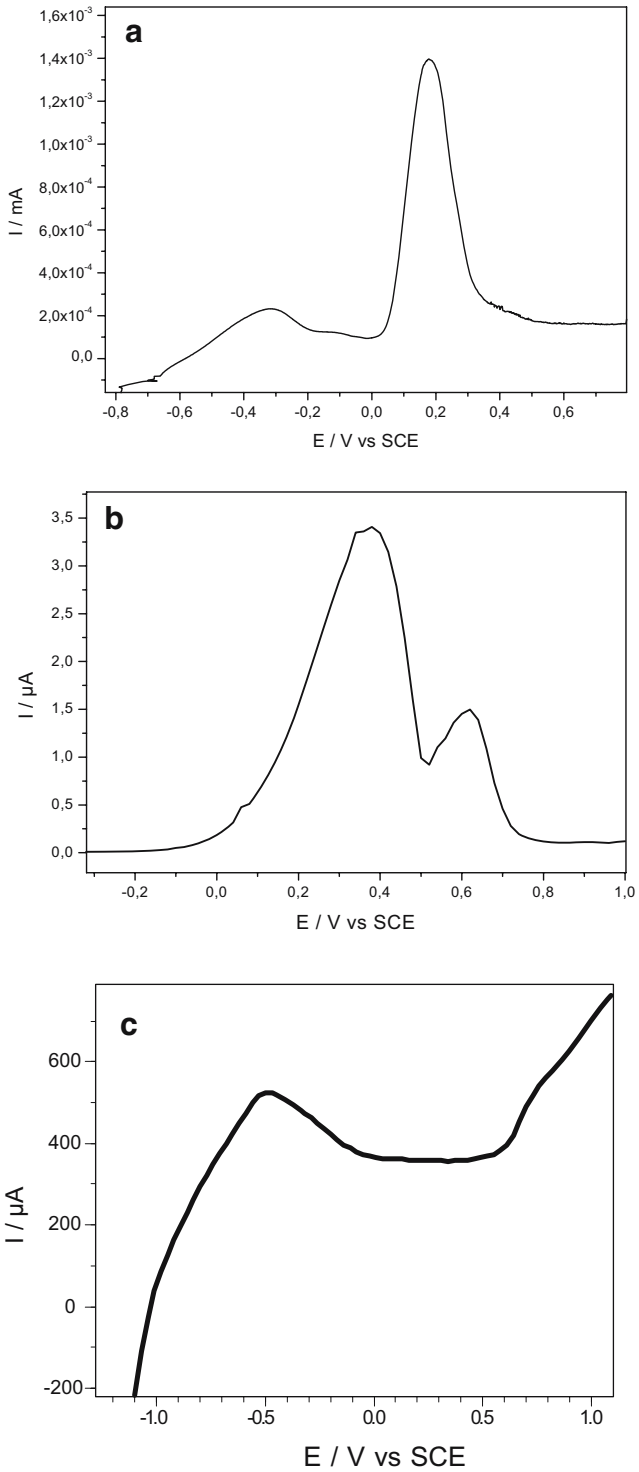

Fig. 4 Polarization behavior of NiCu film (**a**), NiCo film (**b**), and nickel film (**c**) deposited from aqueous solution within the pore of AAO. The spectra were recorded at 3 mV/s in 0.4 M $LiClO_4$

Corrosion measurement

The behavior and performance of metals or alloys films is linked to their chemical composition, phase, and surface

morphology. Measurements such as polarization curves in the form of Tafel plots have been particularly useful and elucidative in corrosion studies [26]. Application of the Tafel equation can give important information such as the corrosion potential, E_{corr}, the corrosion current, I_{corr}, the anodic and cathodic Tafel slopes (β_a, β_c) [27] which are functions of the charge transfer coefficient R_p [28].

$$I_{corr} = \beta_a\beta_c/2.203R_p(\beta_a + \beta_c) \quad (1)$$

Typical polarization curves of NiCo and NiCu films recorded directly after immersion in 0.4 M $LiClO_4$ are shown in Fig. 5. Samples were prepared in the same conditions like that used to obtain Fig. 1b and c and Figs. 2 and 3. In each case, two curves were recorded under the same experimental conditions to ensure that the observed corrosion potential is not due to experimental error. As shown in Fig. 5, each series of corrosion data contains two curves that correspond to two measurements. Both curves are almost in agreement; the error is negligible, as the curves overlap in most cases.

The corrosion potential of NiCu and NiCo films prepared by electrodeposition with aqueous solution and in the presence of liquid crystal (CTAB and Brij 78) is compared in Table 1. In general, the corrosion potentials shifted to negative values when the film was prepared from liquid crystal. This tendency is more pronounced in the film deposited with CTAB surfactant. A corrosion potential of about −479 mV was obtained with NiCu macroscale film deposited from aqueous solution into AAO with a current density of 5 mA/cm^2 during 30 min; this value is more positive compared to that of the same alloy (nanoscale range NiCu sol.) summarized in Table 1. To check if the more negative E_{corr} of film prepared in the presence of CTAB is due to bromide ions or an eventual surfactants molecules, the corrosion curves of the alloy deposited with mixture A were first recorded in 0.4 M $LiClO_4$ and secondly in a mixture of 0.4 M $LiClO_4$ and 0.05 M CTAB. It was observed that the corrosion potential (~−0.520 V) shift anodically to about 0.1 V vs SCE in the second solution. Therefore, the negative E_{corr} of the sample deposited from liquid crystal is not due to surfactant or bromide ions. Furthermore, the corrosion of cobalt nanofilm prepared in the pore of AAO with similar experimental conditions was also investigated.

It appears from Fig. 6 that the corrosion potential of cobalt film deposited in the presence of surfactant shifted to negative value. Moreover, Yamauchi et al. [25] observed anomalous behavior during the electroless synthesis of NiCo mesoporous alloy from lyotropic liquid crystalline (Brij56) media. That is the suppressed deposition of nickel leading to higher cobalt content irrespective of the nature of the plating media such as aqueous solution or aqueous solution containing highly concentrated surfactants addi-

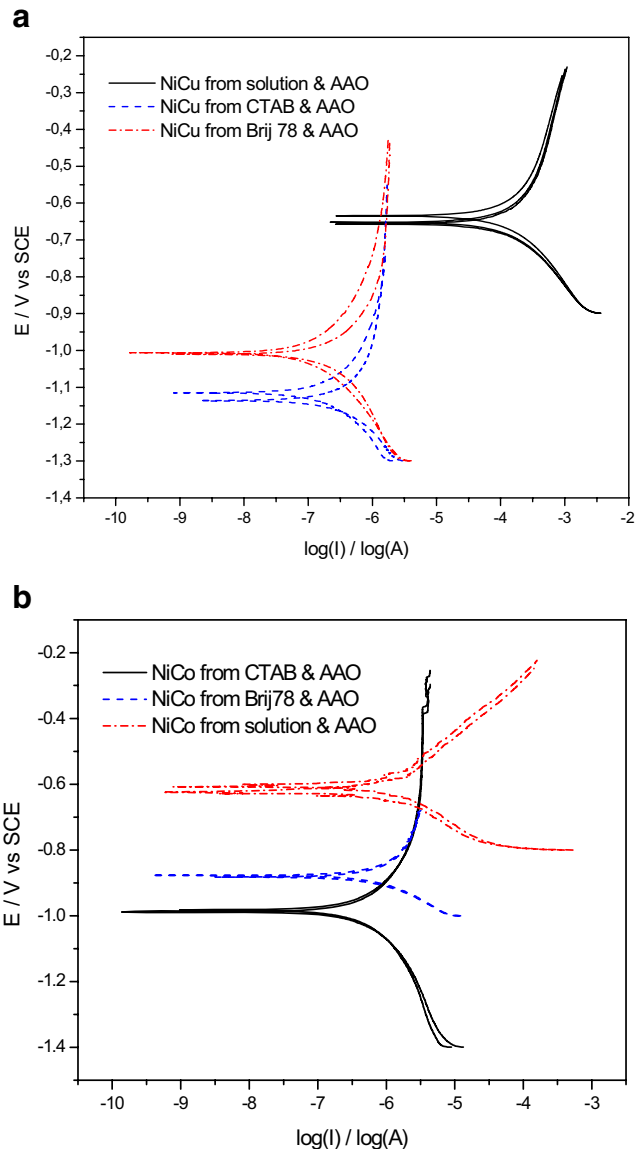

Fig. 5 Polarization curve of NiCu and NiCo alloy nanofilms. Each graph shows the differences between the corrosion curves of films prepared with aqueous solution and that obtained in the presence of Brij 78 or CTAB liquid crystal. Spectra were recorded at 3 mV/s in 0.4 M $LiClO_4$ aqueous solution. Electrode area, 0.196 cm^2

tive. In any case, the composition of the product can be varied by the compositions of the plating solutions even under the presence of highly concentrated surfactants [25]. These observations suggested that the negative potential observed in the case of NiCo and NiCu cannot be assigned

Table 1 Corrosion potential of NiCo and NiCu alloy nanofilm deposited with aqueous solution (subscript A), in the presence of Brij 78 (subscript B), and CTAB (subscript C)

Alloy	$NiCo_A$	$NiCo_B$	$NiCo_C$	$NiCu_A$	$NiCu_B$	$NiCu_C$
$E_{corr/V\ vs\ SCE}$	−0.60	−0.88	−0.99	−0.63	−1.00	−1.12

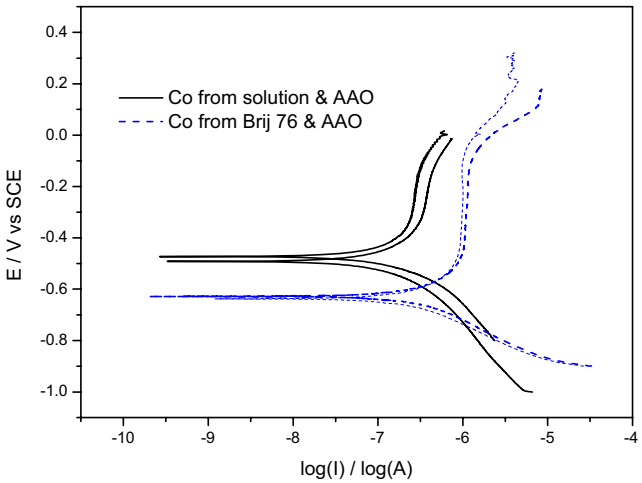

Fig. 6 Polarization of curves of cobalt nanofilm deposited in the pore of AAO. The graph shows the differences between the E_{corr} of cobalt films deposited from aqueous solution and that obtained in the presence of liquid crystal

to the change of composition when the surfactant is introduced.

Considering Tafel analysis and AFM/STM results, the following items could explained the observations. The first is the nanofilms formation process, that is, the nature of the plating mixture used for deposition. The second is the morphology of particles. Fine complicated structures often change the dissolution and film formation behavior of metals and alloys. Particles with small size are easier to oxidize compared to larger particles. The specific area also increases when the surface is made of very small particles, and the films become more catalytic; hence, the displacement of the corrosion potential toward negative values.

A close look at the polarization results and the corrosion curves show that the active dissolution of the film takes place, in all cases, at a potential greater (more anodic) than E_{corr}. That is in good agreement with theory; the relation between the pitting potential (potential at which active dissolution begins) and the corrosion potential of a metal is as follows [29].

$$E_P = E_{corr} + \Phi + \eta \quad (2)$$

Where Φ is the potential induced by the migration of ions and, η the polarization need to reach the critical pit initiation current density.

Electrochemical impedance spectroscopy

EIS was used to study the interface properties of NiCo and NiCu films in 0.4 M $LiClO_4$ at potential below the pitting potential. The resistance and capacitance contributions from various phases (electrode grain boundary, interface double layer capacitance) can be derived from EIS spectra analysis [30]. The spectra were recorded with 5-mV ac amplitude of sinusoidal voltage in the frequency range from 100 kHz to 5 Hz with 10 pt/decade.

Figure 7 gives the complex-plane representation of the impedance data of NiCo and NiCu alloy nanofilm prepared from aqueous solution. A depressed capacitive loop is observed in the high-frequency region, while a straight line

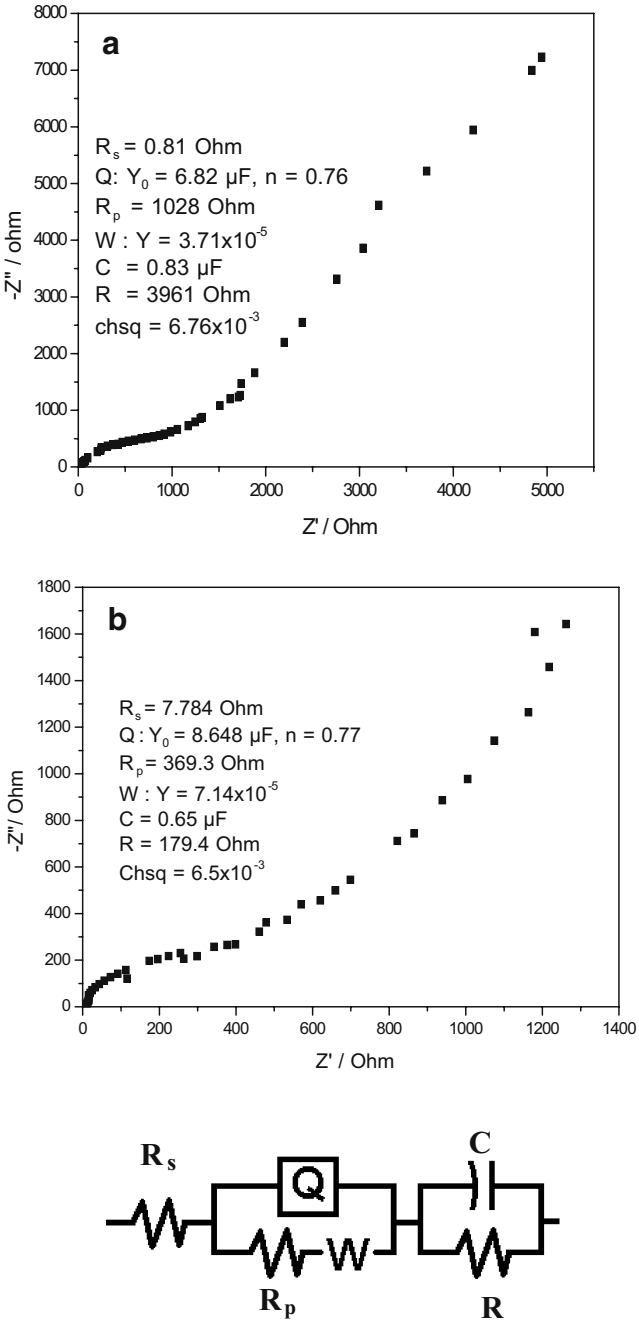

Fig. 7 Nyquist representation of the impedance data of NiCu (**a**) and NiCo (**b**) alloy nanofilm deposited from solution to the pore of AAO. The applied dc potential was −0.7 V and −0.5 V vs SCE for NiCu and NiCo film, respectively. The electric parameters deduced by fitting with the equivalent circuit are displayed in each graph

appears at low frequency. This straight line is assigned to the diffusion in the pore present on the film. Recent study shows that the diffusion process is controlled by the diffusion of diluted oxygen from the solution to the electrode [31].

The impedance data were fitted with the equivalent circuit of Fig. 7 using the ZsimDemo 3.2 simulation software operating with non-linear least square algorithm. The high-frequency loop accounts for two physical processes with very close time constant. The first time constant (R, C) could be assigned to the relaxation process in the $NiCo/Al_2O_3$ or $NiCu/Al_2O_3$ composite or to the eventual oxide film and its dielectric properties. It can also be assigned to the space charge capacitance. Rehim et al. [32] and Nigam et al. [33] reported that a surface film could be considered to be a parallel circuit of resistor due to the ionic conduction in the oxide film, and a capacitor due to its dielectric properties. The medium frequency time constant (Q, R_p) is attributed to the polarization resistance (R_p) and the double layer capacitance (Q) at the film electrolyte interface. The values of the double layer capacitance represented in the model by the constant phase element $\left[Z_Q = Y_0^{-1}(j\omega)^{-n}\right]$ are, in all cases, greater than the film capacitance C. Similar curve shape was obtained with samples prepared from CTAB, but the impedance magnitude was higher compared to this cases.

Conclusion

In the present work, surfactants were used to control the deposition of nanomaterial. The principle of double template electrochemical method was developed to prepare NiCo and NiCu magnetic alloy nanofilms. Well-ordered alloy nanorods were obtained by direct reduction of ions from an aqueous solution within the pore of alumina membrane on aluminum. The combination of the hexagonal phase of a liquid crystal and AAO leads to nanofilms with double subdivisions; one due to the pores of AAO and the other to the columns of liquid crystal. Particles of sizes less than 5 nm were deposited with Brij 78, CTAB, and AAO. The anodic linear voltammetry confirms the presence of nickel, cobalt, or copper elements on each surface. The corrosion potential of the alloys seems to depend on the size of particles; films deposited in the presence of CTAB and AAO have smaller particle size and more negative corrosion potential compared to that deposited directly from solution into AAO.

Acknowledgements The Deutsche Forschungsgemeinschaft and the Land Sachsen-Anhalt financially supported this work.

References

1. Myung NV, Nobe K (2001) J Electrochem Soc 148:C136
2. Qin J, Nogués J, Mikhaylova M, Roig A, Muñoz JS, Muhammed M (2005) Chem Mater 17:1829
3. Prieto AG, Fdez-Gubieda ML (2004) Physica B 354:92
4. Soler MAG, Da Silva SW, Garg VK, Oliveira AC, Azevedo RB, Pimenta ACM, Lima ECD, Morais PC (2005) Surf Sci 575:12
5. Bettge M, Chatterjee J, Haik Y (2004) Biomagn Res Technol 2:1
6. Myung NV, Park DY, Yoo BY, Sumodjo PTA (2003) J Magn Magn Mater 265:189
7. Pattanaik GR, Pandya DK, Kashyap SC (2002) J Electrochem Soc 149:C363
8. Weihnacht V, Péter L, Tóth J, Pádár J, Kerner Z, Schneider CM, Bakonyi I (2003) J Electrochem Soc 150:C507
9. Guo L, Leobandung E, Chou SY (1997) Science 27:649
10. Iwasaki T, Motoi T, Den T (1999) Appl Phys Lett 75:2044
11. Zheng MJ, Zhang LD, Li GH, Zhang XY, Wang XF (2001) Appl Phys Lett 79:839
12. Piao Y, Lim H, Ghang JY, Lee WY, Kim H (2005) Electrochim Acta 50:2997
13. Khan HR, Petrikowski K (2002) Mater Sci Eng C19:345
14. Bartlett PN, Gollas B, Guerin S, Marwan J (2002) J Phys Chem Chem Phys 4:3835
15. Nandharkumar I, Elliott JM, Attard GS (2001) Chem Mater 13:3840
16. Elliott J, Attard GS, Bartlett PN, Coleman NRB, Merckel DAS, Owen JR (1999) Chem Mater 11:3602
17. Masuda H, Fukada K (1995) Science 268:1466
18. Attard GS, Leclerc SAA, Maniguet S, Russel AE, Nandharkumar I, Gollas BR, Bartlett PN (2001) Microporous Mesoporous Mater 44–45:159
19. Nelson PA, Elliott JM, Attard GS, Owen JR (2002) Chem Mater 14:524
20. Kossyrev PA, Yin A, Cloutier SG, Cardimona DA, Huang D, Alsing PM, Xu JM (2005) Nano Lett 5:1978
21. Ozbay E (2006) Science 311:189
22. Whitehead AH, Elliott JM, Owen JR, Attard GS (1999) Chem Commun (Camb) 4:331
23. Doshi DA, Gibaud A, Goletto V, Lu M, Gerung H, Ocko B, Han SM, Brinker CJ (2003) J Am Chem Soc 125:11646
24. Zečević SK, Zotović JB, Gojković SL, Radmilović V (1998) J Electroanal Chem 448:145
25. Yamauchi Y, Yokoshima T, Momma T, Osaka T, Kuroda K (2004) J Mater Chem 14:2935
26. Alves VA, Paquim AMC, Cavaleiro A, Brett CMA (2005) Corros Sci 47:2871
27. Flitt HJ, Schweinsberg DP (2005) Corros Sci 47:2125
28. Maji BC, Das CM, Krishnan M, Ray RK (2006) Corros Sci 48:937
29. Galvele JR (2005) Corros Sci 47:3053
30. Song SG, Ling Z, Placido F (2005) Mater Res Bull 40:1081
31. Ma HY, Yang C, Chen SH, Jiao YL, Huang SX, Li DG, Luo JL (2003) Electrochim Acta 48:4277
32. Rehim SSAE, Hassan HH, Amin MA (2002) Appl Phys Sci 187:279
33. Nigam AK, Balasubramaniam R, Bhargava S, Baligidad RG (2006) Corros Sci 48:1666